# SHAPE MEMORY ALLOY ACTUATED MICRO-FLOW EFFECTORS FOR VORTEX MANIPULATION

F.C. Wong, C.A. Rabbath, N. Hamel, D. Corriveau
Defence R&D Canada - Valcartier
Quebec, Qc, Canada
Contact: franklin.wong@drdc-rddc.gc.ca

O. Boissonneault
Numerica, Quebec, Qc

N. Léchevin
Université du Québec à Trois-Rivières, Quebec, Qc

S. Chen
Institute of Aerospace Research
National Research Council of Canada, Ottawa, On

Received August 2006, Accepted March 2007
No. 06-CSME-36, E.I.C. Accession 2955

## ABSTRACT

Smart structures are seen as an enabling technology for designing innovative control actuation systems for future missiles. In this study, the feasibility of employing shape memory alloy (SMA)-actuated micro-flow effectors to control the vortex shedding behaviour that produces side forces on slender body missiles is examined. Supersonic wind tunnel tests were performed on a slender finless missile equipped with static micro-flow effectors on a conical nose to determine suitable configurations that could generate significant side forces. Shape memory alloy actuators for the flow effector were developed using numerical techniques and validated experimentally. Matching the force-displacement characteristics of the SMA actuator to the micro-flow effector force-displacement requirement was accomplished by a compliant transmission mechanism. The dynamic performance of the micro-flow effector was assured with a two-step variable structure control law. Closed-loop test results showed that the control law was capable of providing effective displacement control up to 1.0 Hz.

# MICRO-EFFECTEURS ACTIONNÉS PAR ALLIAGES À MÉMOIRE DE FORME POUR LA MANIPULATION DES TOURBILLONS

## RÉSUMÉ

Les structures intelligentes sont perçues comme une technologie qui permet la conception de systèmes d'actuation innovateurs pour les missiles de demain. Dans cette étude, la faisabilité des micro-effecteurs actionnés par un alliage à mémoire de forme (AMF) a été examinée. Ces micro-effecteurs servent à la commande des tourbillons qui produisent les forces latérales aux missiles. Les tests ont été effectués dans une soufflerie supersonique avec un missile effilé et sans ailette. Le missile a été doté de micro-effecteurs statiques sur une nez conique pour déterminer les configurations qui peuvent générer des forces latérales significatives. Les actionneurs AMF ont été développés avec les techniques numériques et validés expérimentalement. Les caractéristiques en force et déplacements de l'actionneur AMF ont été harmonisé avec les comportements exigés par le micro-effecteur en utilisant une transmission élastique. La performance dynamique du micro-effecteur a été assurée par une loi de commande variable en deux étapes. Les résultats en boucle fermée ont montré que la loi est capable de contrôler efficacement le déplacement du micro-effecteur jusqu'à 1 Hz.

## 1. INTRODUCTION

New technologies in aerospace are often developed to increase the speed, range and maneuverability of aerovehicles while reducing the volume and weight of its components. Flight control actuation systems for missiles, for example, have been improved with the introduction of electromechanical systems to replace large hydraulic or pneumatic systems. More recently, systems using smart structures concepts have been examined to replace traditional control actuation systems (1), (2). If small control surfaces can be placed at strategic locations on the body to influence the macroscopic downstream flow, it is possible to create large aerodynamic forces that affect the body's attitude. Patel (3) demonstrated the effectiveness of eight deployable flow effectors to control the vortex shedding that produces yaw forces on a subsonic missile. The flow effectors were situated concentrically on a missile nose cone and located 41 mm from the tip. The flow effectors measured 9 mm long by 0.8 mm wide by 3 mm high and were deployed 1 mm into the airstream by a pneumatic actuation system. Massey (4) showed that small pin flow effectors could be employed to modify shock wave structures for supersonic projectile trajectory control. The pins were located at the aft-end of the projectile and were displaced 3.3 mm into the airflow by a rocker mechanism and a pneumatic actuator. Along similar lines, Patel (5) established the feasability of using spoilers that were situated on the boattail of a subsonic projectile to promote flow separation as a means for flight control. The arc-shaped flow effectors varied in length from 10 to 50 mm and in height from 1 to 2 mm. Actuation was achieved using electromechanical solenoids.

In Refs. (3) to (5), attention was focused on finding the flow effector configurations that would allow significant aerodynamic forces to be generated through the manipulation of flow structures. Little was done to develop a lightweight actuation system that could fit in constrained space of a missile or projectile to actuate the flow effector. Smart structures based on materials such as shape memory alloys offer the opportunity to create compact, solid-state actuation systems by virtue of the material's ability to convert electrical energy to mechanical energy within its microstructure. In this study, a nose-mounted flow effector actuation system to alter vortex shedding behaviour and subsequently control the side forces on slender missiles is presented. First, the aerodynamic basis for the flow effector's geometry, force and displacement requirements is provided. Then, issues concerning the actuator behaviour and design of the force-displacement transmission mechanism are discussed. Finally, the method used to obtain closed-loop control of the flow effector displacement is presented.

## 2. BACKGROUND

A wind tunnel and computational fluid dynamic (CFD) study was performed to determine the geometry and actuation requirements for a flow effector configuration that could alter vortex shedding structures to produce significant side forces on a missile body at moderate angles-of-attack.

### 2.1 Wind Tunnel Model

The baseline missile configuration is shown in Fig. 1. The model consisted of a cylindrical body having a diameter of 30 mm and length of 300 mm with a conical nose that was 90 mm long. Trapezoidal-shaped flow effectors measuring 2.67 mm long by 1 mm high by 0.79 mm thick were selected to disturb the flow along the nose and to create asymmetries that would induce side forces. Since the flow effectors were small in relation to the nose diameter and length, they were called micro-flow effectors.

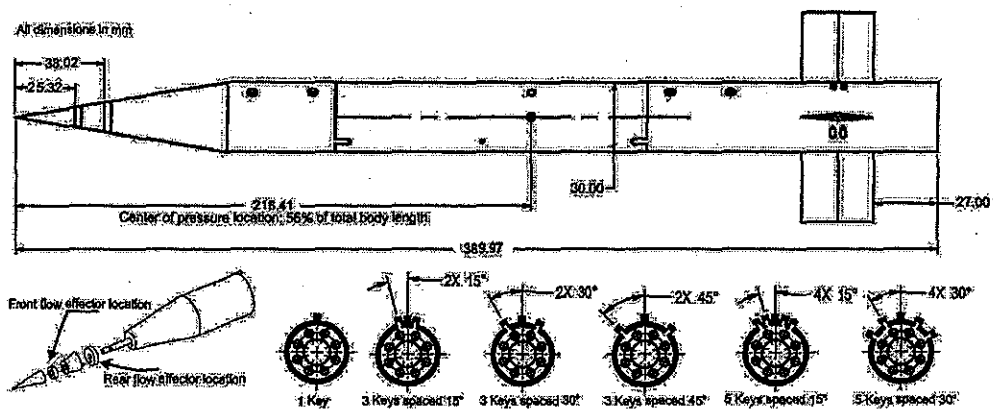


Figure 1: Missile and Flow Effector Configurations

The nose cone was equipped with disks onto which different configurations of static micro-flow effectors (also called keys) were mounted. The nose-disk assembly was designed such that the disks could be indexed in 45 deg. steps. One disk is located at a distance of 25.32 mm from the nose tip whereas a second row of micro-flow effectors is situated at 38.02 mm from the tip. For the purposes of this discussion, only the results of the single micro-flow effector, clean body (no fins) configuration will be shown. Discussion of the complete aerodynamic study may be found in (6) and (7).

## 2.2 Experimental and Numerical Results

Aerodynamic data were obtained at a supersonic flow condition of Mach 1.5 for angles-of-attack between 0 and 20 deg. The results for the measured side force coefficients are shown in Fig. 2 for different micro-flow effector angular positions as measured clockwise from the z-axis. Depending on the angular location of the flow effector, the magnitude of the side force coefficient varied between 0.06 to 0.70. Furthermore, the variation in side force was symmetric for flow effector configurations located at complementary angular positions (e.g. 90 and 270 deg.). The lateral force coefficients increased as the angle of attack increased with peak magnitudes occuring at an angle-of-attack between 15 and 20 deg. Following the peak, a reduction in lateral force was observed for all configurations. The asymmetry in the magnitude of the side forces in the figure when comparing the port and starboard data is thought to be caused a micro-asymmetry in the model and is not related to the micro-flow effectors themselves.

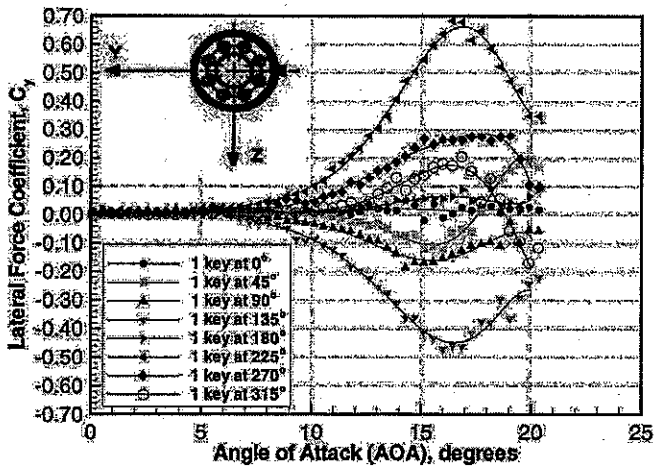


Figure 2: Lateral force coefficient variation with angle-of-attack for one key located at various angular positions 25.32 mm from the nose tip.

CFD computations were made using the Spalart Allmaras turbulence model in the FLUENT (8) and SPARC (9) codes on the wind tunnel model with micro-flow effectors positioned at 225 deg. and 270 deg. Figure 3 shows that the downstream pressure distribution between the port and starboard side of the missile model with the presence of the micro-flow effector is significantly different. Examination of the streamline results revealed that the micro-flow effector triggers the primary vortex structure earlier on its side of the body causing it to grow more rapidly than the vortex on the opposite side of the body. Thus, the micro-flow effector does not generate the control forces by itself but is able to induce a flow asymmetry whose integrated effect is useful for controlling the flight of a missile.

Figure 3: Pressure contours along missile body at AoA = 17 deg. for flow effectors placed at 270 deg. (top) and 225 deg. (bottom) angular positions. Nose cone is on righthand side of the diagram.

The aerodynamic study demonstrated that it was feasible to develop a control actuation system based on a micro-flow effector concept. Table 1 summarizes the dimensions of the flow effector required for the missile model and the worst case external force that would act on the effector. The air conditions for a supersonic flow of Mach 1.5 are provided for reference. It is particularly important that the actuator be able to drive the flow effector 1 mm up into the flow.

**Table 1.** Micro-flow effector specifications and operating environment

| Item | Parameter | Value |
|---|---|---|
| Micro-flow effector dimensions | l - length (mm) | 2.667 |
| | w - width (mm) | 0.787 |
| | h - exposed height (mm) | 1.0 |
| Aerodynamic conditions | M - Mach | 1.5 |
| | $\rho$ - air density (kg/m$^3$) | 0.441 |
| | S - micro-flow effector surface (l x w, mm$^2$) | 2.099 |
| | $C_D$ - drag coefficient | 2.0 |
| | V - velocity (m/s) | 431 |
| Aerodynamic loading | $F_{aero} = \frac{1}{2} \rho S C_D V^2$ (N) | 0.172 |

## 3. SMA ACTUATION OF MICRO-FLOW EFFECTORS

Shape memory alloys (SMA) have one of the highest energy density ratings of all the functional materials (10). Its ability to generate relatively large forces and displacements are attractive for microactuator applications. However, its slow response has imposed some limitations on its widespread use (11). Shape memory alloys are complex materials where an inter-relationship exists between the grain characteristics and external conditions such as force, displacement and temperature. To understand this inter-relationship and its implications for missile control applications, a micromechanical approach (12) was taken to account for the effects grain orientation and texture and combined with a macroscopic approach to account for the transformation kinetics (13), (14). Model predictions and experimental methods were used to determine the operating parameters for a SMA actuator. A summary of the SMA actuator model is presented in Sec. 3.1 with experimental validation results given in Sec. 3.2.

### 3.1 Constitutive and Thermal Model

At the macroscopic level, the global SMA strain is described by a Reuss-type rule of mixtures law

$$\varepsilon_{ij} = (1-\Phi)\varepsilon_{ij}^{A} + \Phi\varepsilon_{ij}^{M} \tag{1}$$

where $\varepsilon$ is the global strain, $\Phi$ is the total martensite fraction, $\varepsilon^A$ is the strain in the austenite phase and $\varepsilon^M$ is the strain in the martensite phase.

Assuming that the strains remain within the linear elastic limits of the SMA, the elastic strain in the austenite is given by the usual linear thermo-elastic constitutive equation

$$\varepsilon_{ij}^{A} = \frac{1}{E^{A}}\left[(1+\upsilon^{A})\sigma_{ij} - \upsilon^{A}\delta_{ij}\sigma_{kk}\right] + \delta_{ij}\alpha_{ij}^{A}\Delta T \tag{2}$$

where $E^A$ is the austenite elastic modulus (Pa), $\upsilon^A$ is the austenite Poisson ratio, $\sigma$ is the applied stress (Pa), $\alpha^A$ is the austenite thermal expansion coefficient ($K^{-1}$). The strains due to thermal expansion are neglected because they are small relative to the transformation strains.

The martensite strain consists of an elastic component (eq. 2, except martensite materials properties are used), a stress-induced phase transformation component and a temperature-induced phase transformation component. Previous studies have shown that the dilatational strains due to the irreversible one-way shape memory effect (SME) are small so the temperature-induced martensite has not been included here. The martensite strain is

$$\varepsilon_{ij}^{M} = \varepsilon_{ij}^{el} + \frac{\Phi^{\sigma}}{\Phi}\varepsilon_{ij}^{\sigma} \tag{3}$$

where $\varepsilon^{el}$ is the elastic strain, $\varepsilon^{\sigma}$ is the stress-induced strain and $\Phi^{\sigma}$ is the stress-induced martensite fraction. The total martensite fraction is

$$\Phi = \Phi^{T} + \Phi^{\sigma} \tag{4}$$

where $\Phi^T$ is the temperature-induced martensite fraction.

The stress-induced strain, $\varepsilon^{\sigma}$, is a preferential deformation of the martensite variants in response to an external stress. The strain is given by

$$\varepsilon_{ij}^{\sigma} = \frac{1}{N}\sum_{n=1}^{N} f^{n}(\theta_1,\theta_2,\theta_3) R_{ik}^{n} R_{jl}^{n} \varepsilon_{kl}^{\sigma n} \tag{5}$$

where $N$ is the number of grains, $f^n(\theta_1,\theta_2,\theta_3)$ is a frequency distribution function, $R_{ik}^{n}R_{jl}^{n}$ is the coordinate rotation matrices that rotate the local grain coordinate system to the global coordinate system and $\varepsilon^{\sigma n}$ is the average stress-induced variant strain of grain $n$ in the local coordinate system (15).

The martensite transformation kinetics is defined on a global basis using the model proposed by (13). The model parameters are quantified by a critical stress-temperature diagram (see Fig. 8) derived from constant temperature tensile tests carried out over a temperature range $T<T_{Mf}$ to $T>T_{Af}$ where $T_{Mf}$ is the martensite finish temperature (K) and $T_{Af}$ is the austenite finish temperature (K). The stress-induced martensite fraction is calculated as a function of critical stress at a specific temperature. The martensite fraction versus critical stress relationship is described using a linear function in the form of a Heaviside model as proposed in (16). Others have used trigonometric functions (17) or exponential functions (18) to describe the stress-induced phase transformation.

The temperature-induced martensite fraction, $\Phi^T$, is assumed to be linearly dependent on temperature between the martensite start and finish temperatures.

$$\Phi^{T} = \frac{T_{Ms} - T}{T_{Ms} - T_{Mf}} \tag{6}$$

where $T_{Ms}$ is the martensite start temperature and $T_{Mf}$ is the martensite finish temperature. The stress-induced martensite will form even if $T>T_{Ms}$. Therefore the fraction of temperature-induced martensite is subject to the inequality

$$\Phi^T \leq 1-\Phi^\sigma \tag{7}$$

Assuming the shape memory alloy is a wire with a large length to diameter ratio and is uniformly heated from resistive heating, the one-dimensional heat transfer equation for heat flow in the radial direction including exo- and endothermic behaviour is (19), (20)

$$\rho V\left(C_p\frac{dT}{dt}-H\frac{d\Phi}{dt}\right)=\frac{E^2}{R_{el}}-h_{th}(T-T_a) \tag{8}$$

where ρ is density (kg/m$^3$), $V$ is the wire volume (m$^3$), $C_p$ is specific heat (J/kg K) and $H$ is latent heat of formation (J/kg), $E$ is the applied voltage (V), $R_{el}$ is the wire resistance (ohms), $T$ is the wire temperature (K), $T_a$ is the ambient temperature (K), $h_{th}$ is the convective thermal conductance (W/K).

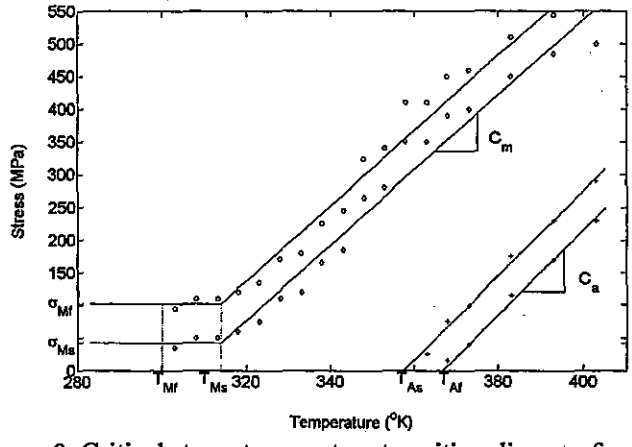


Figure 8: Critical stress-temperature transition diagram for 0.1 mm dia. SMA wire.

## 3.2 Experiments

A 0.1 mm diameter NiTi as-drawn wire with critical stress-temperature behaviour as shown in Fig. 8 was selected for the experimental work. The pull force and austenite finish temperature were listed to be 150 g and 80 to 90°C, respectively. Experiments were carried out for SMA wires that were arranged as an agonistic-antagonist pair. Load cells were attached to the ends of each 0.1 mm SMA wire. One end of a thin nylon cord was connected to the SMA wire common junction with the other end attached to a LVDT to record displacement.

The antagonistic actuator was modelled using the theory presented in Sec. 3.1. An iterative method was used to calculate the equilibrium displacement-stress pairs at each time step. The common junction displacement, temperature and martensite fraction were calculated for each wire independently as a function of initial temperature, stress and voltage. If the difference between the two common junction

displacements exceeded a tolerance value, the initial stress would be adjusted until the predicted common junction displacement difference was within an acceptable error.

The numerical and experimental results for a [2V, 0.1Hz] and [3V,0.25Hz] are shown in Figs. 9 and 10, respectively. The common junction displacement for 2V and 3V behaved like a first-order system where no overshoots or oscillations are present. The plateau in displacement indicated that the wires had sufficient time to fully heat or cool.

It can be seen in Figs. 9 and 10 that a phase shift and displacement magnitude difference exists between the predicted and experimental displacement results. The cause of these discrepancies were traced back to the cooling behaviour of the SMA wire. Figure 11 shows the stress-strain behaviour of the SMA wire as it was cycled at 30°C. For wires exhibiting an irreversible shape memory effect, an increase in deformation would be accompanied by a linear increase in stress until the critical martensite start stress is reached. It can be seen that during the initial loading stage deformation occurred at zero stress. This behaviour is indicative of the reversible shape memory effect (RSME) where an alloy returns to its initial length only through cooling in the absence of a restoring force (21). The presence of the RSME resulted in the model overestimating the stresses required to return the common junction to its reference position. According to the transition diagram (Fig. 8), higher predicted stresses must be accompanied by higher temperatures. According to eq. 8, for the same energy flow rate at a higher differential temperature, the incremental time must also increase. Consequently, the time lag in the predicted displacements was caused by the resultant longer cooling time that corresponded to an over-prediction of the wire stress and temperature. At the lower voltage and lower frequency, the heating was lower and the dissipation time was longer so the effects of over predicting the stress was minimal. At the higher voltage and frequency, the influence of the two-way shape memory effect on the overall dynamic behaviour was more pronounced so the ability of the model to correctly predict the transient displacement behaviour was degraded. The model can be improved by modifying eq. 5 to account for deformation due to temperature-induced martensite.

The experiments demonstrated that a displacement of ±2 mm was achievable with the 0.1 mm dia. SMA wire. This displacement is more than adequate to actuate a flow effector, however, a frequency response of 0.1 Hz was considered inadequate for the planned proof of concept wind tunnel trials. Further experiments showed that the frequency of the actuator could be increased by reducing the amplitude of the actuator displacement or by simultaneously increasing the voltage amplitude and shortening its duration. The specific voltage-time pulse would depend on the transmission mechanism linking the SMA actuator to the flow effector.

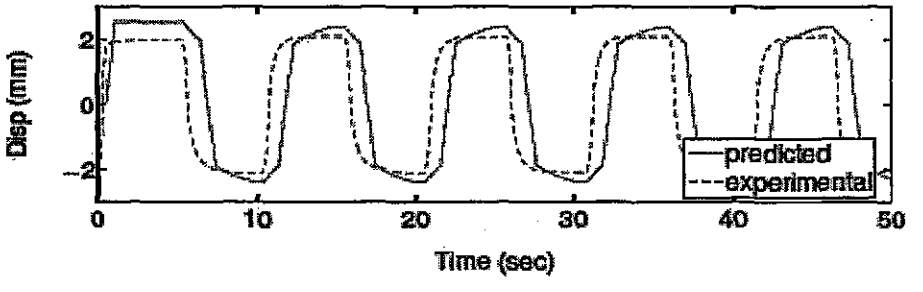


Figure 9: Open-loop results for an antagonistic SMA actuator subjected to a 2V square wave excitation at 0.1 Hz.

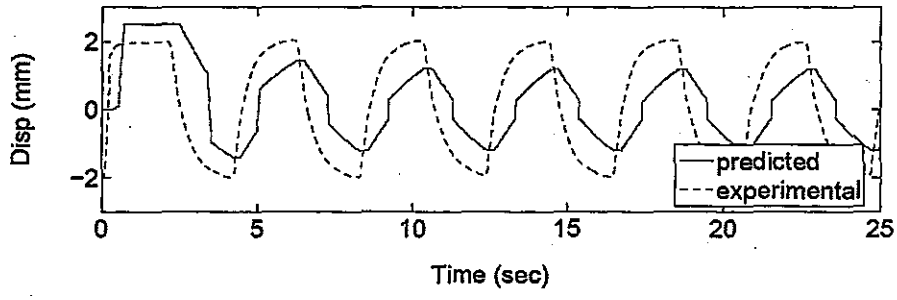


Figure 10: Open-loop results for an antagonistic SMA actuator subjected to a 3V square wave excitation at 0.25 Hz.

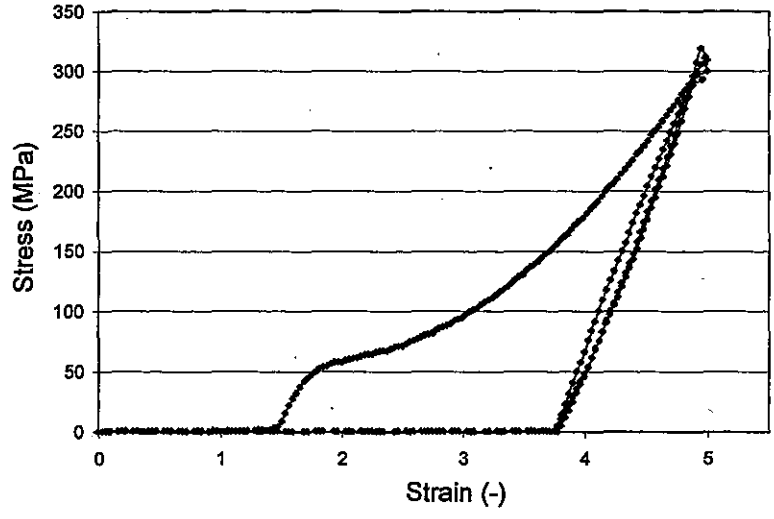


Figure 11: Two-way shape memory effect for SMA wire strain-cycled at 30C.

## 3.3 Micro-Flow Effector with Compliant Link

Compliant mechanisms are a class of pivotless structures that transform input force and displacement to a corresponding output force and displacement while attempting to maximize mechanical efficiency. The constraints for the compliant mechanism linking the SMA actuator to the flow effector are: 1) the tip of the micro-flow effector must displace 1 mm in the upward direction while being subjected to a maximum aerodynamic load of 0.172 N, 2) the selected SMA wire can generate >150 g force at voltages starting from 0.5 VDC and 3) the maximum length of the SMA wire is 100 mm due to missile body volume constraints.

A parametric model (Fig. 12) for a 787 micron thick micro-flow effector was built in the ANSYS programming language. The flow effector is actuated by applying a force at the locations '$F_{SMA\ top}$' or '$F_{SMA\ bot}$'. The optimized geometry had to minimize the bending stresses in the compliant link for a maximum SMA force of approximately 150 g while maximizing the tip displacement at '$F_{Aero}$'. The critical dimensions of the mechanism are: 1) the compliant link dimensions 'TOPWID', 'BASWID' and 'L4HGT' because they control the link stress level and the maximum displacement magnitude, and 2) the

lever arm ratio 'L2LEN' to 'L1LEN' and 'THGT' because they control the amplification of the horizontal displacement at '$F_{SMA\ top}$' or '$F_{SMA\ bot}$' to the upward tip displacement at '$F_{Aero}$'. The dimensions 'ARMWID' and 'LEVHGT' play a lesser role in the mechanism. If they are too small, the structure becomes too flexible under load. Figure 13 shows an example of the overall deformation behaviour of a mechanism for a force applied at the location '$F_{SMA\ top}$'.

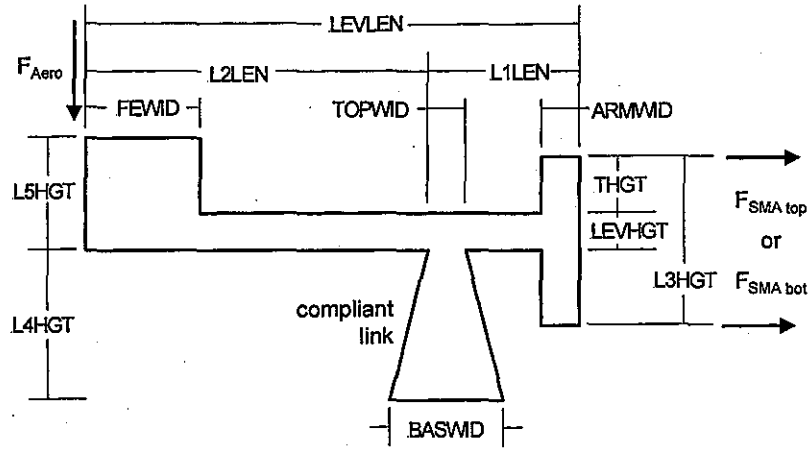


Figure 12: Nomenclature for trapezoid compliant mechanism dimensions.

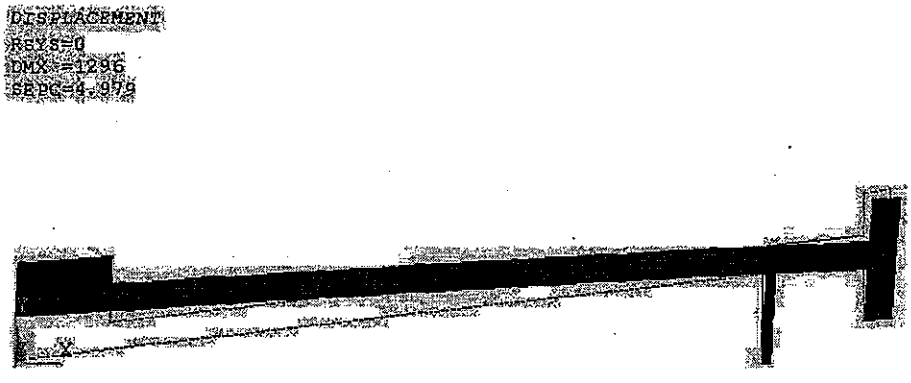


Figure 13: Displacement plot of flow effector mechanism with a force applied at $F_{SMA\ top}$.

A total of thirty eight geometries were analysed in the parametric study. It was found that the compliant link, when fabricated from aluminum, would yield if the flow effector tip displaced the required 1 mm. This result suggested that a link fabricated from a material such as titanium would be necessary if it was to survive all operating conditions. The change to titanium resulted in a thinner link design that required a higher voltage input to generate an actuator force of 185 g to account for the increased stiffness of the titanium relative to aluminum. Table 2 lists the dimensions of an optimized micro-flow effector and the expected performance. If the mechanism was operated under quiescent

conditions, the micro-flow effector tip would displace by 1.817 mm for an actuator displacement of 0.367 mm giving a mechanical advantage of 5. The compliant link would reach 90% of its yield stress capacity. Under aerodynamic loading, the tip displacement would decrease to 1.011 mm for an actuator displacement of 0.240 mm giving a mechanical advantage of 4.2. Since the bending stresses are related to the tip displacement, the link reaches only 72% of its yield stress capacity.

The optimized mechanism requires an actuator displacement of 0.240 mm. If the maximum actuator strain is set at 1%, the actuator wire would need to have a minimum length of 24 mm. Therefore, the proposed mechanism summarized in Table 2 would meet the SMA force, the flow effector displacement, the missile body volume and the link material constraints.

**Table 2:** Dimensions of and expected performance for the optimized micro-flow effector mechanism

| Parameter | Value | Performance | Value |
|---|---|---|---|
| L1LEN (micron) | 3607 | $F_{SMA}$ top only | |
| L2LEN (micron) | 21158 | SMA disp (micron) | +367 |
| L3HGT (micron) | 3429 | Effector tip disp (micron) | +1817 |
| L4HGT (micron) | 2540 | Effector post stress (MPa) | 799 |
| L5HGT (micron) | 2286 | Mechanical advantage | 5.0 |
| TOPWID (micron) | 254 | $F_{SMA}$ top plus $F_{Aero}$ | |
| BASWID (micron) | 279 | SMA disp (micron) | +240 |
| ARMWID (micron) | 762 | Effector tip disp (micron) | +1011 |
| LEVHGT (micron) | 762 | Effector post stress (MPa) | 635 |
| FEWID (micron) | 2667 | Mechanical advantage | 4.2 |
| LEVLEN (micron) | 24765 | | |
| THGT (micron) | 1207 | | |

If the flow effector was actuated only with a fixed voltage pulse, inaccurate tip displacements, and as a consequence, inaccurate manipulation of the vortex shedding structure and subsequent aerodynamic forces would result because of the nonlinear nature of the SMA actuator. To regain accurate position performance, a closed-loop control scheme is needed to ensure fast and accurate displacement of the flow effector tip. An essential component of the closed-loop system is a feedback sensor that measures tip displacement. The results of the finite element parametric study revealed that a one-to-one correspondence existed between the flow effector tip displacement and the compliant link bending strains. Feedback sensors consisting of two semi-conductor strains gages measuring 0.5 mm long by 0.3 mm wide were attached on opposite sides of the compliant link at the base and wired in a half-bridge configuration to measure the bending strains as the flow effector tip displaced vertically. The Wheatstone bridge was completed with dummy resistors and a temperature-compensation resistor that would provide a balanced output over a 38°C to –45°C temperature range. To verify the accuracy of the finite element strain predictions, an instrumented flow effector was subjected to a series of loads to simulate the SMA actuator forces that would generate a range of tip displacments. Figure 14 shows that there is close agreement between the theoretical and experimental results. A slight nonlinear behaviour is evident in the

experimental results. It is thought that this nonlinearity is caused by bondline creep at loads over 175 g. Since actuator forces of 185 g are required under wind-on conditions, it will be necessary to minimize the time that the bondline is subjected to the high stresses to minimize creep. Alternatively, a new curing schedule for the epoxy adhesive could be developed to increase its creep resistance.

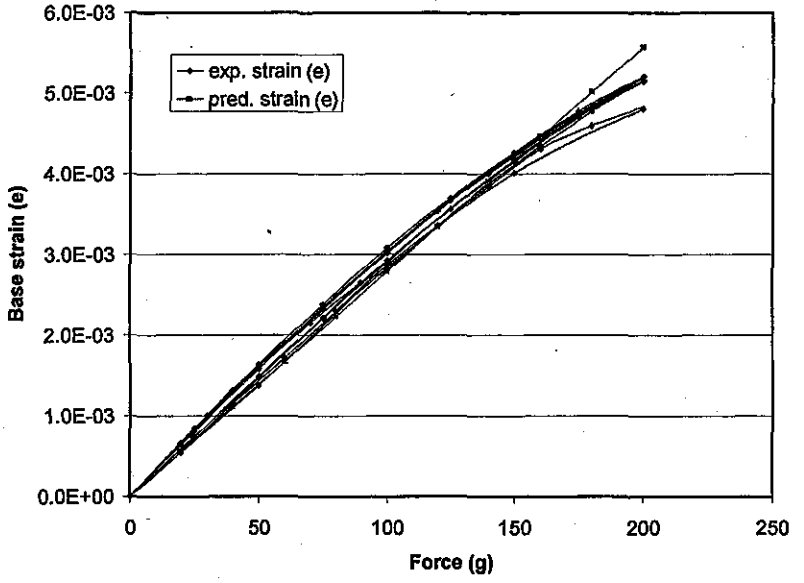


Figure 14: Validation of finite element predictions of compliant link strains for a series of SMA forces.

## 4. POSITION CONTROL OF SMA ACTUATION

As mentioned in the previous section, the flow effector requires closed-loop control to obtain a fast and accurate displacement response. To this end, a digital controller was designed with the objective of controlling the effector position of an SMA actuation mechanism over a range of 1 mm and within a bandwidth of [0 Hz, 1 Hz]. To meet these requirements, a variable structure set-point regulator is proposed. The controller is comprised of two parts. First, to warrant fast transients, a bang-bang controller is activated whenever the regulation error is above a fixed threshold. Second, a linear digital controller is switched on when the error reaches the threshold. The linear digital controller provides smooth convergence of the closed-loop system to the steady state and prevents high frequency chattering, which is typical of bang-bang control.

The plant under digital control is comprised of the compliant flow effector, the SMA wires, the power drive and the control electronics (Fig. 15). Since the micromechanical model of the SMA actuator was not designed for control studies, parameter identification of the actuated flow effector was first carried out. Then, the discrete-time linear plant model obtained was used to design the digital controller that matched pole-placement requirements of a reference closed-loop continuous-time system with the objective of achieving zero steady-state error. It is important to stress that SMA wires are characterized by nonlinear behaviour in the form of hysteresis and dead zones, and may reach saturation. Cruz-Hernandez and Hayward (22) showed, however, that a linear time-invariant filter in parallel with a rate-independent hysteresis, which is represented by a phase-lag shift module, provides a modelling that is suitable to achieve satisfactory hysteresis compensation at low frequencies. Although the phase lag is actually a

function of the magnitude of the controller output, we simplify the problem by assuming a constant phase lag characterization. First, a nonparametric identification of the SMA was achieved. Then, the phase bode plot was used to devise a phasor, i.e. a phase compensator that compensates for the delay induced by the hysteresis over a specific bandwidth. The parameter identification adopted in this paper is the parametric equivalent of the approach proposed in (22). Experimental results show that the two-step variable structure controller satisfies the required specifications.

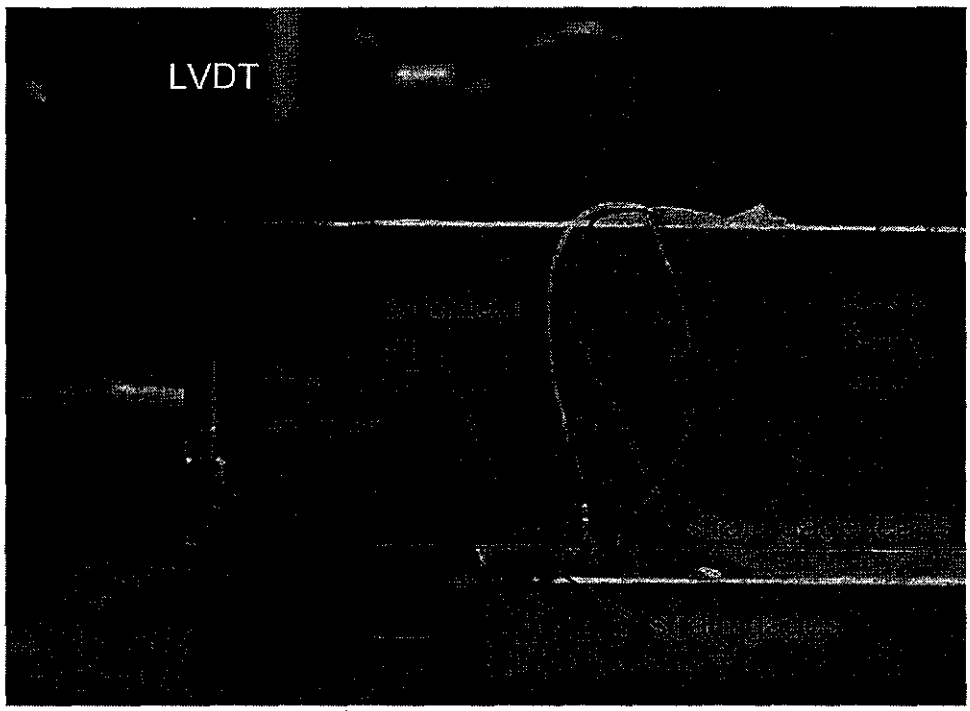


Figure 15: Actuated micro-flow effector test set-up. The flow effector mechanism measures 24.765 mm long.

## 4.1 Two-step variable structure controller

The proposed controller builds upon a control synthesis method proposed in a previous work (23), where the control law is comprised of a bang-bang-like control, $C_1$, approximated by a hyperbolic function in series with a proportional-derivative law $C_2$, as shown in Fig 16 (a), where $\theta$ and $\theta_d$ denote the actual and desired positions.

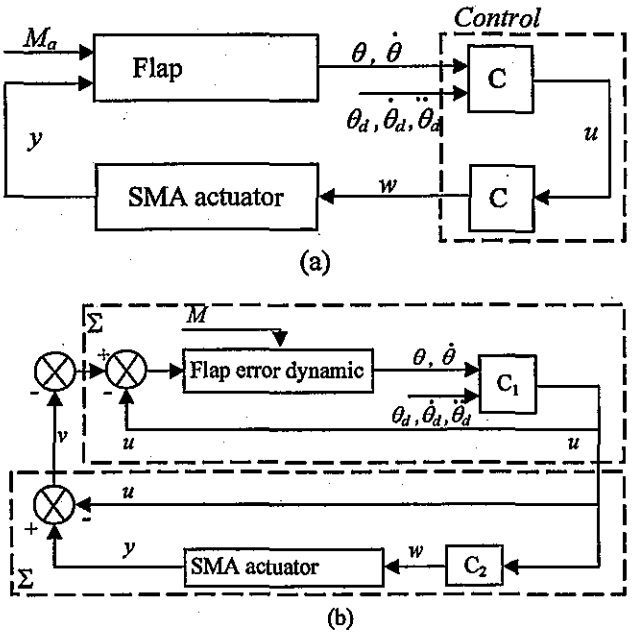


Fig. 16. Structure of the quasipassivity-based control law (23). (a) Control law decomposition in $C_1$ and $C_2$. (b) Passive feedback decomposition.

The control law $(C_1,C_2)$ is shown to be ultimately uniformly bounded by means of quasipassivity arguments in (23), (24); that is, $C_1$ and $C_2$ are synthesized to render the forward and feedback loops $\Sigma_1$ and $\Sigma_2$, depicted in Fig. 16(b), strictly quasipassive. $\Sigma_1$ passivates and stabilizes the plant by assuming an ideal SMA actuator, whereas $\Sigma_1$ compensates for the phase lag induced by the hysteretic behavior of the SMA and thus can be interpreted as a phase-lead compensator. By the quasipassivity theorem (24), the system trajectories approach a ball $B(\theta_d,r)$ as $t\to\infty$, where the radius $r$ depends on the total memory of the alloy, according to the Krasnoselskii and Prokrovskii's model in (24). Radius $r$ can be reduced by increasing the controller gains provided chattering is avoided. To obtain zero steady-state error while avoiding the chattering effect, we propose to modify the quasipassivity-based control law of (23) so that the controller can switch from the $(C_1,C_2)$ operating mode to an integral action control law that ensures a set-point regulation without chattering, as shown in Fig. 17.

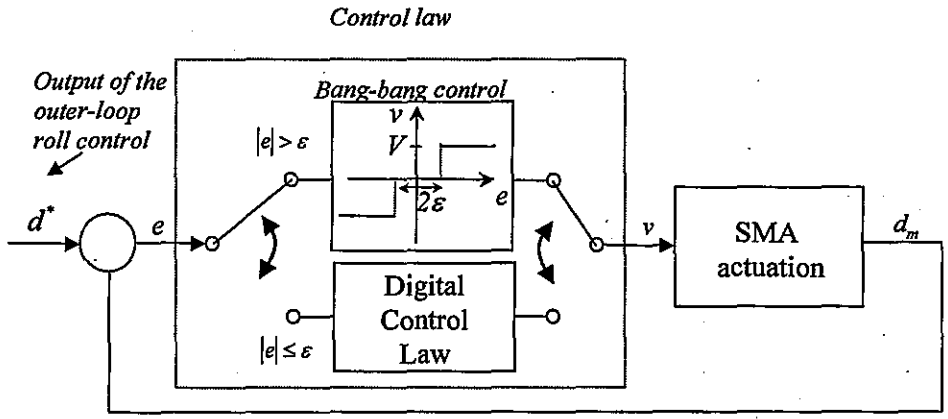


Figure 17: Variable structure control of the SMA actuation

The controller depicted in Fig. 17 is a two-step variable structure control law comprising:

- A bang-bang control, $v = V\text{sign}(e)$, which is triggered whenever $|e|$ is greater than a threshold ε.
- A discrete-time control law designed from the parameter identification of the plant, which ensures set-point regulation near the equilibrium. The latter discrete-time control law is implemented to prevent the chattering usually found with bang-bang control.

The choice of the threshold ε results from a trade-off between a large value to avoid fast switching from one controller to another and a small value to warrant reliable computation of the controller's state-space variables at the switching time. In fact, a small ε indicates that the closed-loop system is close to its steady state, which can be easily obtained from the well-known final value theorem.

## 4.2 Parameter identification of SMA actuator

The system to be identified is comprised of:

- A digital board, comprising a signal conditioning module that interpolates data to linearize $(v, v_1)$ and $(v, v_2)$ characteristics;
- Analogue electronic devices that select the SMA wire to heat;
- SMA wires (1) and (2);
- Micro-flow effector with compliant link.

The controller output provides voltage $v_1$ and $v_2$ which induce displacement $d_m$. The system from the voltage reference trajectory $v$ (volt), which is the output of the discrete-time control law implemented on the digital board, to the displacement $d_m$ (mm) is identified. Model identification is achieved offline by selecting $v$ as a chirp signal and by measuring and storing signal $d_m$. Such experiments are conducted for several chirp signals characterized by a voltage magnitude $V_a$ in [0.5 V, 4.5 V] and a bandwidth of [0.1 Hz, 1Hz].

Each series of data, corresponding to a specific $V_a$, is used for model parameter identification. Time constants of the whole dynamics, which is mainly composed of the heat transfer dynamics and the compliant mechanism dynamics, are expected to be larger than 100 ms. The sample period $T_s$ is 10 ms. Such a period is used for data acquisition, parameter identification, and corresponds to the update period of the digital control law. A $T_s$ of 5 ms is sufficiently small to model the dynamics of interest without

overloading the acquisition and computing capabilities of the computer. The autoregressive ARX model (eq. 9) is used for parameter identification (25).

$$y(t)+a_1y(t-1)+...+a_{na}y(t-na)=b_1u(t-d)+...+b_{nb}u(t-d-nb+1) \tag{9}$$

where input $u$ and output $y$ represent voltage $v$ and displacement $d_m$, respectively; $n_a$ is the number of poles; $n_b$-1 is the number of zeros and $d$ is the pure delay, assumed to be an integer multiple of $T_s$. The identification is performed according to the following algorithm:

```
FOR each Va  GET (v, dm)
    FOR  na = 1 to 5
        FOR  nb = 1 to 5
            FOR d = 1 to 5                                              (10)
                (a1,...ana, b1,..., bnb) = ARX(v, dm, na, nb, d)
END END END END
```

This algorithm is implemented under Matlab Identification Toolbox. Iterations performed in eq. 10 are intended to give a set of parameters that provide the best fitting ratio. Only fitting ratios greater than 80 % are considered.

## 4.3 Discrete-time control of the actuator

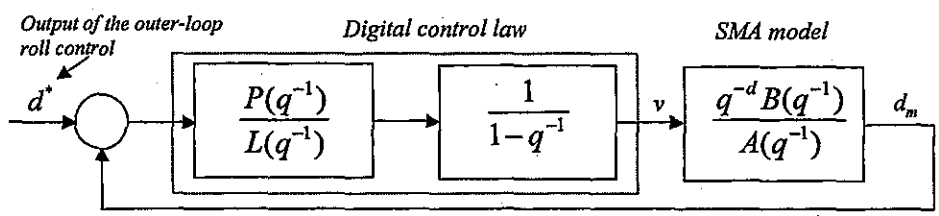


Figure 18: SMA discrete-time control in the vicinity of the steady state

A direct digital design approach (26) that ensures pole placement of the closed-loop system is adopted and leads to the computation of coefficients $l_0, l_1, l_2, p_0, p_1, p_2$ in polynomials $L(q^{-1})$ and $P(q^{-1})$. The discrete-time control law, as shown in Fig. 18, is comprised of an integrator $1/(1-q^{-1})$ in series with $P(q^{-1})/L(q^{-1})$. The model of the plant in series with the integrator yields $q^{-1}B(q^{-1})/\overline{A}(q^{-1})$ where $\overline{A}(q^{-1})=(1-q^{-1})A(q^{-1})$ and $B(q^{-1})=b_1+b_2q^{-1}$. Polynomial $A(q^{-1})$ is of degree two. Henceforth,

$$\begin{aligned}&\overline{A}(q^{-1})=(1-q^{-1})(1+a_1q^{-1}+a_2q^{-2})\\&1+(a_1-1)q^{-1}+(a_2-a_1)q^{-2}-a_2q^{-3}\\&=\overline{a}_0+\overline{a}_1q^{-1}+\overline{a}_2q^{-2}+\overline{a}_3q^{-3}.\end{aligned} \tag{11}$$

The model of the closed-loop system can be written as

$$\frac{d_m}{d^*} = \frac{q^{-d}PB}{L\bar{A} + q^{-d}BP} = \frac{q^{-d}PB}{A^*} \tag{12}$$

where $A^*(q^{-1})$ is a polynomial of degree 5. Let $z_i = e^{s_i T_s}$, for $i$=1,...5, the zeros of $A^*$. Therefore, poles of the closed-loop transfer function $d_m/d^*$ are equal to $z_i$, $i$=1...5, if the coefficients of $L(q^{-1})$ and $P(q^{-1})$ and satisfy the following system 26 when $d$=1

$$\begin{bmatrix} \bar{a}_0 & 0 & 0 & 0 & 0 & 0 \\ \bar{a}_1 & \bar{a}_0 & 0 & b_1 & 0 & 0 \\ \bar{a}_2 & \bar{a}_1 & \bar{a}_0 & b_2 & b_1 & 0 \\ \bar{a}_3 & \bar{a}_2 & \bar{a}_1 & 0 & b_2 & b_1 \\ 0 & \bar{a}_3 & \bar{a}_2 & 0 & 0 & b_2 \\ 0 & 0 & \bar{a}_3 & 0 & 0 & 0 \end{bmatrix} \begin{bmatrix} l_0 \\ l_1 \\ l_2 \\ p_0 \\ p_1 \\ p_2 \end{bmatrix} = \begin{bmatrix} a_0^* \\ a_1^* \\ a_2^* \\ a_3^* \\ a_4^* \\ a_5^* \end{bmatrix} \tag{13}$$

where $a^*_i$, for i=1,...5, are such that

$$\begin{aligned} A^*(q^{-1}) &= a_0^* + a_1^* q^{-1} + a_2^* q^{-2} + a_3^* q^{-3} + a_4^* q^{-4} + a_5^* q^{-5} \\ &= (q^{-1} - z_1)(q^{-1} - z_2)(q^{-1} - z_3)(q^{-1} - z_4)(q^{-1} - z_5) \end{aligned} \tag{14}$$

The identified model gives rise to undershoot that is caused by unstable zeros. It was found that locating dominating poles of $d_m/d^*$ at $s_1 = s_2 = -3$, while $s_3 = s_4 = s_5 = -30$, gave satisfactory responses in terms of the rise time and the transients.

## 4.4 Experimental results

The two-step variable structure controller was implemented on a LabView platform with a sample period of 10 ms. The voltage applied to the SMA wires was generated by a pulse width modulator (PWM), whose switching frequency was 400 Hz. The output voltage of the PWM for the bang-bang control was approximately 3 V while the discrete-time control voltage was approximately 0.8 V. Figure 19 shows typical set-point-regulated flow effector position schedules that would be used in wind tunnel tests. The actuator under feedback control shows fast responses during the rising part of the motion and zero steady error. Furthermore, there is no chattering because the digital controller replaces the bang-bang law for small tracking errors. The response time is less than 0.3 sec with an overshoot of about 5% of the steady state value. It is clear from Fig. 19(b) that the response time of the motion from 1 mm to 0 mm is longer than that of the rising transient. The difference between the rising and the descending phases is mainly due to the longer cooling time required by the SMA wires. When the heat transfer rate was increased by forced convection, a frequency of 1 Hz was easily attained. A slight increase in response time by 0.2 sec was obtained through the use of the asymmetric antagonistic SMA wire arrangement.

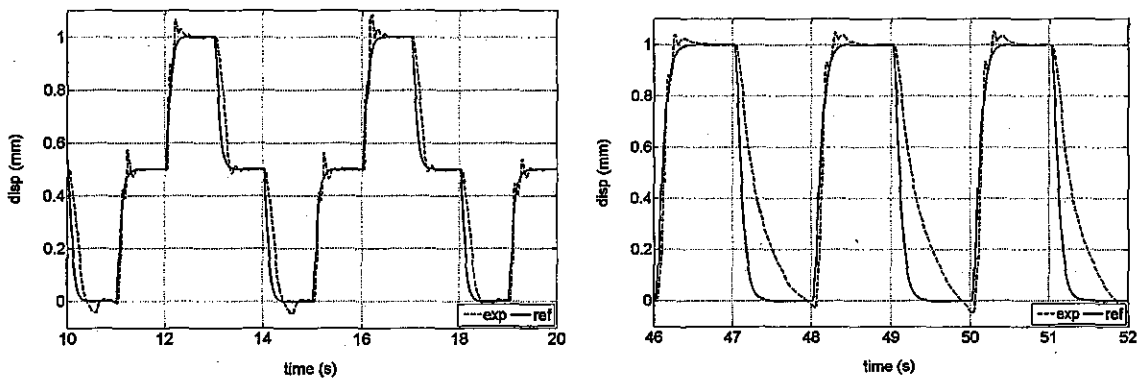


Figure 19: Experimental results of the SMA micro-flow effector set-point regulation.
(a) piecewise constant command of 0.25 Hz; (b) Square wave of 0.5 Hz.

## 5. CONCLUSIONS

A study was carried out to examine the feasibility of employing shape memory alloy-actuated micro-flow effectors to control the vortex shedding structure that produce side forces on slender body missiles. Wind tunnel tests on a missile model showed that useful side forces could be generated with static micro-flow effectors. Shape memory alloy (SMA)-actuated micro-flow effectors were developed to achieve active side force control. The numerical SMA actuator displacement results compared well with the experimental data though the presence of the reversible shape memory effect in the SMA wire caused the stress and temperature behaviour to be overpredicted. Matching of the SMA actuator to the flow effector kinematic requirements was accomplished through a compliant mechanism. A two-step variable structure control law consisting of a bang-bang and discrete-time controller was synthesized. Closed-loop test results showed that the proposed SMA micro-flow effector control scheme was capable of providing effective displacement control up to 1.0 Hz.

## 6. FUTURE WORK

Future work will focus on wind tunnel testing the missile model with a gang of position controlled micro-flow effectors. A four micro-flow effector assembly covering angular positions 90, 135, 225 and 270 deg. is being fabricated. The flow effectors at the different angular positions will be actuated as the missile model is pitched through various angles of attack to study transient vortex shedding and side force control. Methods to increase actuator response times in the cooling phase will be investigated. In particular, the compliant transmission geometry will be re-examined to investigate whether a larger mechanical advantage for the bottom SMA wire can be obtained from the asymmetric moment arm to speed the flow effector displacement response.

## ACKNOWLEDGEMENTS

This work was financed by the Defence R&D Canada Technology Investment Fund under the project "Supersonic Missile Flight Control by Manipulation of the Flow Structures using Micro-Actuated Surfaces".

## 7.0 REFERENCES


1. Barrett, R., (1996) "Active aeroelastic tailoring of an adaptive Flexspar stabilator", *Smart Mater. Struct.*, Vol. 5, pp. 723-730.
2. Barrett, R., Stutts, J., (1997) "Modeling, design and testing of a barrel-launched adaptive munition", *4th SPIE Symp. on Smart Structures and Materials*, San Diego, CA, March.
3. Patel, M., Tilmann, C.P., Ng, T.T., (2004) "Closed-Loop Missile Yaw Control via Manipulation of Forebody Flow Asymmetries", *J. Spacecraft and Rockets*, Vol. 41, No. 3, pp. 436-443.
4. Massey, K.C., McMichael, J., Warnock, T., Hay, F., (2004) "Design and Wind Tunnel Testing of Guidance Pins for Supersonic Projectiles", *23rd Army Science Conference*, Orlando, FL, Paper D0-01, Nov.
5. Patel, M.P., Lopera, J., Ng, T.T., (2004) "Active Boattailing and Aerodynamic Control Fins for Maneuvering Weapons", *2nd AIAA Flow Control Conference*, Portland, OR, Paper AIAA 2004-2696, July.
6. Corriveau, D., Hamel, N., Wong F.C., (2006) "Side Force Generation Mechanism on a Missile with Nose-Mounted Micro-Structures", AIAA 2006-3000, *24th Applied Aerodynamics Conference*, San Francisco, CA, June.
7. Chen, S., Khalid, M., (2005) "Numerical Studies for Slender Body Flight Control using Flow Effectors", *CFD2005*, St. John's, Newfoundland, July.
8. FLUENT 6.1 User's Guide, Fluent Inc. (2003) Fluent Inc.
9. Magagnato, F., (1999) "SPARC, Structure Parallel Research Code", Department of Fluid Machinery, University of Karlsruhe, Karlsruhe, Germany.
10. Wolfe, T.B., Faulkner, M.G., Walfaardt, J., (2005) "Development of a shape memory alloy actuator for a robotic eye prosthesis", *Smart Mater. Struct.*, Vol. 14, pp. 759-768.
11. Elahinia, M.H., Ahmadian, M., Ashrafiuon, H., (2004) "Design of a Kalman filter for rotary shape memory alloy actuators", *Smart Mater. Struct.*, Vol. 13, pp. 691-697.
12. Patoor, E., Eberhardt, A., Berveiller, M., (1988) "Thermomechanical Behaviour of Shape Memory Alloys", *Arch. Mech.*, Vol. 40, pp. 775-794.
13. Brinson, L.C., (1993) "One-Dimensional Constitutive Behavior of Shape Memory Alloys: Thermomechanical Derivation with Non-Constant Material Functions and Redefined Martensite Internal Variables", *J. Intell. Mater. Syst. Struct.*, Vol. 4, pp. 229-242.
14. Huang, W., (1999) "Modified Shape Memory Alloy (SMA) Model for SMA Wire Base Actuator Design", *J. Intell. Mater. Syst. Struct.*, Vol. 10, pp. 221-231.
15. Wong, F.C., Boissonneault, O., Terriault, P., (2005) "Hybrid Micro-Macro-mechanical Constitutive Model for Shape Memory Alloys", *Proc. 12th SPIE Int. Symposia on Smart Structures and Materials*, Paper 5761-55, March.
16. Terriault, P., Volkov, A., Trochu, F., (2003) "Chap. 16 Structure-Analytical Model" in **Shape Memory Alloys: Fundamentals, Modeling and Applications**, V. Brailovski, S. Prokoshkin, P.Terriault, F. Trochu Eds., Université du Québec, École de technologie supérieure, pp. 586-615.
17. Liang, C., Rogers, C.A., (1992) "Design of Shape Memory Alloy Actuators", *J. Mech. Design*, Vol. 114, pp. 223-230.
18. Jayender, J., Patel, R.V., Nikumb, S., Ostojic, M., (2005) "H-infinity Loop Shaping Controller for Shape Memory Alloy Actuators", *Proc. 44th IEEE Conf. on Decision and Control and European Control Conf. 2005*, Seville, Spain, December.
19. Shanin, A.R., Meckl, P.H., Jones, J.D., Thrasher, M.A., (1994) "Enchanced Cooling of Shape Memory Alloy Wires Using Semiconductor Heat Pump Modules", *J. Intell. Mater. Syst. and Struct.*, Vol. 5, pp. 95-104.

20. Bhattacharyya, A., Lagoudas, D.C., Wang, Y., Kinra, V.K., (1995) "On the role of thermoelectric heat transfer in the design of SMA actuators: theoretical modeling and experiment", *Smart Mater. Struct.*, Vol. 4, pp. 252-263.
21. Prokoshkin, S.D., (2003) "Chap. 4 Shape Memory Effects" in **Shape Memory Alloys: Fundamentals, Modeling and Applications**, V. Brailovski, S. Prokoshkin, P. Terriault, F. Trochu Eds., Université du Québec, École de technologie supérieure, pp. 124-125.
22. Cruz-Hernandez, J.M. and Hayward, V., (2001 ) "Phase Control Approach to Hysteresis Reduction," *IEEE Transactions on Control Systems Technology*, Vol. 9, No. 1, pp. 17-26.
23. N. Léchevin, C.A. Rabbath, F.C. Wong et O. Boissonneault, "Quasipassivity-based Robust Nonlinear Flap Positioning Control Using Shape Memory Alloy Micro-Actuators," *Trans. of the Canadian Society for Mechanical Engineering,* Vol. 29, No. 2, pp. 143-162, Invited paper, Special Edition, June 2005.
24. I.G. Polushin and H.J. Marquez, "Boundedness Properties of Nonlinear Quasi-Dissipative Systems," *IEEE Trans Auto. Contr.*, Vol.. 49, No. 12, pp.2257-2261, 2004.
25. Ljung, L., (1999) *System Identification - Theory for the User, Prentice Hall*, Upper Saddle River, N.J., 2nd edition.
26. Astrom, K.J. and Wittenmark, B., (1990) *Computer-Controlled Systems: Theory and Design*, Prentice Hall, NJ.